Ki67 regulates nuclear lipid accumulation at the chromosomal periphery to facilitate chromosome individualization during mitosis

Hsiao-Tang Hu[1], Ueh-Ting Tim Wang[2,3], Bi-Chang Chen[2], Yi-Ping Hsueh[1]*, Ting-Fang Wang[1]*

[1]Institute of Molecular Biology, Academia Sinica, Taipei, 11529, Taiwan; [2]Research Center for Applied Sciences, Academia Sinica, Taipei 11529, Taiwan; [3]Affiliated Senior High School of National Taiwan Normal University, Taipei, 106348, Taiwan.

* Corresponding to Dr. Ting-Fang Wang, email: tfwang@gate.sinica.edu.tw and Dr. Yi-Ping Hsueh, Email: yph@gate.sinica.edu.tw, Institute of Molecular Biology, Academia Sinica, 128, Sec 2, Academia Rd, Taipei, 11529, Taiwan, ROC.

Keywords: Biotin-DHPE, Cell cycle, Perichromosomal layer, Expansion microscopy, Ki67, Nuclear lipid, Phosphatidylserine, TT-ExM.

Abstract

A hallmark of eukaryotic species is having distinct numbers of chromosomes surrounded by a nuclear envelope to separate nuclear transcription and RNA processing from cytosolic translation. In animal and plant cells undergoing open mitosis, the nuclear envelope disintegrates before the chromosomes divide into two daughter cells. To ensure faithful genome inheritance, chromosome individualization is involved in partitioning the fully condensed sister chromatids during mitosis. Ki67, a surfactant-like protein that forms a repulsive molecular brush around each pair of fully condensed sister chromatids during early mitosis, mediates chromosome individualization in vertebrates. Using a modified expansion microscopy methodology called TT-ExM for high-sensitivity and super-resolution imaging of proteins, lipids, and nuclear DNA, we found that intranuclear lipids in COS-7 cells not only are enriched at the chromosome periphery but are also excluded from the chromosome interior in a Ki67-dependent manner. Together with nuclear lipids, Ki67 forms the "chromosomal envelope" that mediates chromosome individualization. The transition from nuclear envelope to chromosomal envelope ensures continued separation of genetic material from cytoplasmic material during open mitosis.

33 ## Introduction

34 Lipids are key biomolecules that form the structures of cell membranes and serve as signaling
35 molecules to regulate cellular responses. In the nucleus, neutral and polar lipids are found in the
36 nuclear envelope (NE), nucleolus, and nuclear matrix [1-3]. These lipids can be synthesized *de novo*
37 in the inner nuclear membrane and nuclear matrix or they can be synthesized first at the
38 endoplasmic reticulum connected to the NE and are then transported into the nucleus [4-7]. Some
39 nuclear lipids form droplets that serve as nucleolar scaffolding structures, splicing speckles, and
40 DNA repair foci [8-10]. In addition to serving as structural components, nuclear lipids also participate
41 in a variety of biological functions, including in transcriptional regulation [11-13], signaling [10, 12, 14],
42 the DNA damage response [10, 14], and protein storage [15, 16]. Therefore, nuclear lipids have multiple
43 activities.

44 Ki67 is a giant nuclear protein comprising 3256 amino acids and it is a well-known marker
45 of cell proliferation [17]. The subnuclear distribution of Ki67 changes significantly during the cell
46 cycle [18]. Ki67 is concentrated in the nucleolus and in some punctate structures during interphase,
47 but it relocates to transparent gel-like structures surrounding condensed chromosomes (termed the
48 perichromosomal layer or chromosomal periphery) during mitosis [18-21]. Based on analyses of Ki67,
49 the perichromosomal layer is thought to isolate (or individualize) sister chromatid pairs from other
50 pairs and to promote efficient interactions with the mitotic spindle during mitosis [22]. Ki67 also
51 excludes the cytoplasm from condensed chromosomes during mitosis [23].

52 The perichromosomal layer mostly originates from the nucleolus [20, 24]. When a cell enters
53 mitosis, the nucleolus dissipates and its components relocate to cover the surface of mitotic
54 chromosomes [20, 24]. In addition to Ki67, other nucleolar components, including nucleolin and
55 ribosomal RNA, are present in the perichromosomal layer [25-27]. Although the nucleolus also

56 contains lipids [10, 28, 29], it is currently unclear if nucleolar lipids also relocate to the
57 perichromosomal layer and contribute to its biological functions. Thus, whether nuclear lipids are
58 present or even enriched at the perichromosomal layer remains an intriguing and important
59 question.

60 Expansion microscopy (ExM) is a super-resolution imaging technology that physically
61 expands biological samples by a factor of four or greater, thereby improving the spatial resolution
62 of optical microscopy [30-33]. The biological sample is first embedded in a hydrogel and then
63 physically crosslinked within it, before undergoing protease digestion so that the biological sample
64 expands isotropically with the hydrogel when it is placed in water [30, 31]. Since its original
65 description, many variations of the ExM protocol have been developed to achieve a resolution
66 comparable to those of electron microscopy, including iterative expansion microscopy (iExM) [34],
67 pan-ExM [35], and iterative ultrastructure expansion microscopy (iU-ExM) [36]. However, concerns
68 have arisen regarding the use of these iterative methods to visualize membranes or lipid-containing
69 subcellular structures due to their use of strong lytic and denaturing reagents such as sodium
70 dodecyl sulfate (SDS) and/or sodium hydroxide (NaOH) [34-36].

71 To visualize both proteins and lipids of cultured mammalian cells at a super-resolution
72 scale, we recently established a modified protocol called TT-ExM that involves application of
73 trypsin and tyramide signal amplification (TSA) technologies. We have demonstrated previously
74 that trypsinization retains convincing fluorescent signals in ExM [32, 33]. A combination of a biotin-
75 conjugated lipid, i.e., biotin-DHPE (N-(Biotinoyl)-1,2-dihexadecanoyl-sn-glycero-3-
76 phosphoethanolamine), and TSA technology clearly labeled the membranes and lipid-containing
77 structures of cells, including mitochondria, the nuclear envelope (NE), endoplasmic reticulum,

78 Golgi apparatus, lipid-containing vesicles in the cytoplasm, and lipid-containing foci in the
79 nucleolus [32]. Notably, we have shown that our system reveals the localization of intranuclear lipid
80 components at the perichromosomal layer of mitotic chromosomes [32]. Accordingly, we speculate
81 that nuclear lipids are involved in the formation of the perichromosomal layer. In this report, we
82 deploy TT-ExM to illustrate the ultrastructural organization of the perichromosomal layer by
83 revealing the distributions of lipids and Ki67 during the cell cycle. Our results indicate that Ki67
84 regulates nuclear lipids at the perichromosomal layer and also cooperates with them to isolate or
85 individualize the various sister chromatid pairs during mitosis.

86

87 ## Results

88 **Application of TT-ExM to observe lipid-containing structures and chromosomes**

89 We used Biotin-DHPE and tyramide-Alexa fluor-555 in TT-ExM to label and visualize nuclear
90 lipids in COS-7 cells [32]. After crosslinking to a hydrogel and trypsinization, the sample swells
91 upon immersion in water. PicoGreen, an ultrasensitive green-fluorescent nucleic acid dye for
92 double-stranded DNA, was used to outline nuclear chromosomal DNA. As previously described
93 [32], after 4-fold expansion, both cytoplasmic components and nuclear structures of COS-7 cells
94 expanded isotropically, regardless of their cell cycle stages (**Figure 1A** before expansion **vs. 1B**
95 after expansion). Lipid-containing structures in the cytoplasm, nuclei (e.g., NEs), and nucleoli
96 were clearly labeled by biotin-DHPE (**Figure 1B**), confirming the feasibility of deploying biotin-
97 DHPE in TT-ExM to reveal cellular lipid structures. Notably, biotin-DHPE signals were present
98 in the peripheral regions of mitotic chromosomes (**Figure 1B**, middle magnified inset), suggesting
99 the presence of lipids in the perichromosomal layer. All images shown in Figure 1 were viewed
100 using a Zeiss LSM700 confocal laser scanning microscope.

101 Next, we applied a Zeiss LSM980 confocal laser scanning microscope with an AiryScan 2
102 area detector to acquire super-resolution images of COS-7 cells stained with 4',6-diamidino-2-
103 phenylindole (DAPI). DAPI is a blue fluorescent DNA stain for which fluorescence is enhanced
104 ~20-fold upon binding to AT-enriched regions of double-stranded DNA. To quantify the
105 fluorescence signals, we drew a perpendicular line across the chromosome periphery of sister
106 chromatid pairs that had fully condensed during mitosis and performed a line scan analysis of
107 DAPI signals along that line (**Figure 2A**). The expansion index of TT-ExM was determined by
108 comparing the average diameter of fully condensed sister chromatid pairs (**Figure 2B**). Our results
109 show that the average diameters before and after expansion were 1.4 μm and 4.9 μm, respectively,
110 representing an expansion index of 3.5 (**Figure 2C**). Since the LSM980 microscope with AiryScan
111 2 has a resolution of approximately 90-120 nm, we estimate that the resolution of our TT-ExM
112 protocol is 25-34 nm after 3.5-fold expansion [33]. Under the same conditions, counterstaining with
113 PicoGreen revealed the highly condensed chromosome axis in the middle of each sister chromatid
114 (indicated by white arrows in **Figure 2D,** right panel). Notably, the surfaces of most, if not all,
115 individual chromatids during mitosis did not appear smooth, supporting that fully-folded
116 chromosomal loops could be observed under our super-resolution conditions (indicated by white
117 asterisks in **Figure 2D**, right panel). These results indicate that TT-ExM is suitable for isotropic
118 expansion of biological macromolecules (e.g., mitotic chromosomes), allowing us to accurately
119 observe the ultrastructures of organelles and subcellular components under an optical microscope.
120

121 **Dynamic distribution of nuclear lipids during mitosis**

122 Ki67 acts in organizing the perichromosomal layers [23, 27]. A previous study has shown that Ki67
123 proteins form a 90-nm-thick perichromosomal layer [22]. Since TT-ExM has a resolution as high as

124 25-34 nm (**Figure 2**), we applied it to analyze the distribution of lipid components in the
125 perichromosomal layers. In addition to biotin-DHPE, we dual-stained the cells with an anti-Ki67
126 antibody (**Figure 3**) and an anti-phosphatidylserine (PS) antibody (**Figure 4**), respectively. The
127 phosphoethanolamine (PE) in biotin-DHPE is a neutral glycerophospholipid, whereas PS is an
128 anionic glycerophospholipid. Immunofluorescence signals of anti-PS antibodies specifically
129 localize in epichromatin throughout the cell cycle and are associated with nucleosome core
130 histones [37]. In fixed and permeabilized cells, epichromatin can be identified by co-
131 immunolocalization of Ki67 with staining signals of particular anti-nucleosome or anti-PS
132 antibodies [38].

133 We observed that the immunofluorescence signals of biotin-DHPE indeed overlapped with
134 those of Ki67 at perichromosomal layers during prometaphase and metaphase (**Figure 3A**). As
135 mitosis progressed into anaphase and telophase, we detected enhanced biotin-DHPE
136 immunofluorescence signals in the chromosomal interior regions. These results indicate that
137 DHPE-labeled nuclear components (e.g., nuclear lipids) had migrated from the perichromosomal
138 layers toward chromosomal cores as mitosis progressed (**Figure 3A**).

139 To quantify the movement of the biotin-DHPE signals toward the chromosomal interior,
140 we performed line scanning as described in Figure 2 to determine the ratio between the lowest
141 biotin-DHPE signal within chromosomes and the biotin-DHPE signal at chromosome edges, i.e.,
142 the inner/edge ratio of DHPE signal (**Figure 3B**). Our results show that this ratio is less than 0.4
143 during prometaphase and metaphase, but increases to ~0.5 and ~0.6 for anaphase and telophase,
144 respectively (**Figure 3C**). By quantifying average global Ki67 immunofluorescence signals in
145 mitotic cells, we also detected that intracellular Ki67 levels decline as mitosis progresses from
146 prometaphase to telophase (**Figure 3D**). Given that we uncovered a significant negative correlation

147 between intracellular Ki67 protein levels and the inner/edge ratio of DHPE signals (**Figure 3E**),
148 we speculate that Ki67 may prevent DHPE-labeled nuclear components (e.g., nuclear lipids) from
149 moving into chromosomal interiors during prometaphase and metaphase, thereby promoting
150 chromosome individualization.
151
152 **Perichromosomal lipid composition and layer organization**
153 Consistent with the previous study [37], we also found that PS immunoreactivity specifically
154 localized in epichromatin after specimen expansion (**Figure 4A**, upper). Z-projection images
155 revealed that PS signal specifically occurred on the surface of the mitotic chromosome cluster
156 during prometaphase (**Figure 4A**, lower). This pattern differs from that of biotin-DHPE signals,
157 which surrounded the mitotic chromosomes (**Figure 4A and 4B**). However, biotin-DHPE signals
158 overlapped with the PS signals within the epichromatin region (**Figure 4B**). Our line scan analysis
159 indicated that the peak of PS signals was closer to the edge of mitotic chromosomes compared to
160 the peak of biotin-DHPE signals (**Figure 4C**). Taken together, these results indicate that, in
161 addition to PS, other lipid components are also enriched around chromosomes.
162 We also analyzed the relative positions of the signal peaks for Ki67 and biotin-DHPE.
163 Similar to our comparison of PS and biotin-DHPE, we found that the peak of Ki67 signals was
164 closer to the edge of mitotic chromosomes compared to the peak of biotin-DHPE signals (**Figure**
165 **4D, 4E**). Thus, the DHPE-labeled lipid layer appears to be located outside of the Ki67 layer of the
166 perichromosomal zone. This scenario is consistent with our hypothesis that Ki67 may prevent
167 inward movement of lipid components into the interior of mitotic chromosomes.
168

169 **Ki67 knockdown causes chromosome aggregation, slows cell cycle progression, and alters**
170 **the pattern of the microtubule array**

171 To further confirm the role of Ki67 in controlling lipid distribution across chromosomes and the
172 perichromosomal layer, we studied the effect of Ki67 knockdown in COS-7 cells. To establish and
173 characterize Ki67 knockdown, we designed a plasmid expressing an artificial miRNA, Ki67-miR,
174 to downregulate endogenous Ki67 in COS-7 cells. Immunostaining and immunoblotting revealed
175 that Ki67-miR significantly reduced Ki67 protein levels in COS-7 cells relative to the control
176 construct Ctrl-miR (**Figure 5A-5C**). Consistent with previous studies [22, 23], Ki67 knockdown
177 prompted mitotic chromosome collapse and aggregation (**Figure 5A**, as revealed by DAPI
178 counterstaining). Quantification analysis revealed that the area occupied by chromosomes was
179 diminished in Ki67 knockdown cells compared to cells expressing Ctrl-miR (**Figure 5D**). These
180 results demonstrate that we had successfully knocked down Ki67 and impaired the spatial
181 arrangement of mitotic chromosomes in COS-7 cells.

182 Ki67 knockdown also delayed the progress of mitosis. First, we applied nocodazole to
183 arrest control or Ki67 knockdown COS-7 cells at prometaphase (**Figure 5E**, left panel). After
184 washing away nocodazole and allowing the cells to recover for 15, 30, or 60 minutes, we then
185 counted the numbers of COS-7 cells at different stages of mitosis (i.e., prometaphase, metaphase,
186 anaphase, and telophase). Within 15 minutes of washing away nocodazole, more than 30% of the
187 control cells progessed from prometaphase into metaphase. By comparison, only 10% of the Ki67
188 knockdown cells entered metaphase under the same treatment (**Figure 5E**). Furthermore, less than
189 10% of Ctrl-miR- and Ki67-miR-expressing cells remained in prometaphase 60 minutes after
190 nocodazole had been washed away, with ~40% of the Ctrl-miR-expressing cells entering telophase.
191 In contrast, only 20% of Ki67-miR-expressing cells progressed to telophase. We detected a slight

192 increase in the percentages of Ki67 knockdown cells in metaphase and anaphase (**Figure 5E**,
193 right). Therefore, Ki67 knockdown delays mitotic progression.

194 In addition to chromosomes, we also monitored microtubule patterns in cells expressing
195 Ki67-miR. Since microtubule patterns change during the different stages of mitosis, we focused
196 on the microtubule array in early prometaphase for our comparison (**Figure 6**). At this stage of
197 mitosis, microtubules form a star-like pattern in the center of the chromosome cluster. We observed
198 microtubule filaments extending from the center to the periphery of the chromosome cluster in
199 control COS-7 cells (**Figure 6A**, upper). However, mitotic chromosomes collapsed in Ki67-miR-
200 expressing cells, so although microtubules still formed a star-like pattern in the center of the
201 chromosome cluster of those cells, the star-like pattern was smaller and more irregular than for
202 control counterparts (**Figure 6A**, lower). To quantify the differences, we performed Sholl analysis
203 [39] to analyze the complexity of microtubules in early prometaphase of control and Ki67
204 knockdown cells (**Figure 6B**). Our Sholl analysis revealed that the number of intersections was
205 greatly reduced in Ki67 knockdown cells (**Figure 6C**), i.e., less than 50% of that enumerated for
206 control cells (**Figure 6D**). We further counted all microtubule filament tips to represent the total
207 number of microtubule filaments in each array, which revealed ~50% fewer microtubule tips in
208 Ki67 knockdown cells compared to control cells (**Figure 6E**). Thus, Ki67 knockdown induces
209 microtubule array abnormalities during mitosis.

210 Consequently, Ki67 is critical for chromosome elongation and individualization during
211 mitosis, both of which are required for microtubule attachment to chromosomes to enable mitotic
212 progression.

213

214 **Ki67 knockdown promotes lipid invasion into condensed chromosomes**

215 Lastly, we applied our Ki67 knockdown system to investigate if Ki67 is involved in the inward
216 movement of lipids into the chromosome interior during mitosis. Since we detected biotin-DHPE
217 signals as being lowest within condensed chromosomes during prometaphase compared to other
218 mitotic stages (**Figure 3**), we solely analyzed the effects of Ki67 knockdown during prometaphase.
219 Given that our miR expression construct coexpresses green fluorescent protein (GFP), we used
220 GFP signal to identify transfected cells in culture (**Figure 7A**). Next, we performed line scans to
221 determine biotin-DHPE signals across chromosomes and the perichromosomal layer. GFP signal
222 was included as a control (**Figure 7B, 7C**). We found that the GFP inner/edge ratio was identical
223 (~0.2) for cells expressing either Ctrl-miR or Ki67-miR (**Figure 7D**), indicating that GFP
224 distribution is insensitive to Ki67 knockdown. In terms of biotin-DHPE signals, the ratio for
225 control cells was ~0.28, whereas this ratio increased to 0.34 for Ki67 knockdown cells (**Figure**
226 **7D**), indicating that Ki67 regulates lipid invasion into condensed chromosomes during mitosis.
227

228 ## Discussion

229 Here, we have applied a super-resolution fluorescence imaging system, i.e., TT-ExM [32, 33], to reveal
230 the dynamic distribution of nuclear lipids during the cell cycle, showcasing the involvement of
231 nuclear lipids in how Ki67 acts in chromosome individualization. Our study also provides three
232 lines of evidence that Ki67 regulates the distribution of nuclear lipids on the outer surface and/or
233 interior of condensed chromosomes. First, although Ki67 and nuclear lipids intermingle in the
234 perichromosomal layer, our application of TT-ExM super-resolution imaging enabled us to dissect
235 the layer organization at the chromosomal periphery, revealing that nuclear lipids or lipid-
236 containing materials are enriched outside of Ki67. Therefore, Ki67 may act as a barrier to prevent
237 nuclear lipids from moving into chromosomal interiors. Second, the enrichment of nuclear lipids

238 at the chromosomal periphery is negatively correlated with total Ki67 protein levels during mitosis.
239 Third, Ki67 knockdown results in nuclear lipids invading the interior of mitotic chromosomes,
240 confirming that Ki67 regulates the distribution of nuclear lipids during the cell cycle.

241 How does Ki67 regulate the distribution of nuclear lipids at the periphery of condensed
242 chromosomes? It has been suggested previously that Ki67 may serve as a surface-active agent
243 (surfactant) to mediate the individualization of sister chromatid pairs [22] and to exclude the
244 cytoplasm from fully condensed chromosomes [23]. Although the respective mechanisms remain
245 unclear, it is reasonable to speculate that nuclear lipids enriched at the chromosomal periphery
246 likely cooperate with Ki67 to facilitate the individualization of sister chromatid pairs during
247 mitosis. The general physicochemical features of Ki67 provide clues to the functional interplay
248 between Ki67 and nuclear lipids. Like many surfactants, Ki67 has an amphiphilic structure. The
249 long N-terminal domain of Ki67 is excluded from chromatin, whereas its short C-terminal LR
250 domain displays strong attraction to chromatin [22]. Moreover, the chromosome separation function
251 of Ki67 is not attributable to a specific protein domain, but is correlated with the size and net
252 charge of truncation mutants that lack secondary structure [22]. Thus, the amphiphilic molecular
253 structure of Ki67 may disperse nuclear lipids or lipid-containing components via a liquid-liquid
254 phase transition mechanism, resulting in their accumulation at the chromosomal periphery.
255 Consistent with this supposition, our TT-ExM super-resolution imaging revealed that Ki67 forms
256 numerous tiny granules on the surface of mitotic chromosomes, rather than presenting a smooth
257 and continuous thin layer (**Figure 3A**). These tiny Ki67-positive granules intermingle with lipid-
258 containing nuclear components on the outer surface of mitotic chromosomes (**Figure 3A**).
259 Accordingly, we suggest that Ki67 proteins and these lipid-containing components collectively

260 form a perichromosomal layer that mediates the individualization of sister chromatid pairs during
261 mitosis.

262 Since the lipid-containing nuclear components also display amphiphilic characteristics, it
263 is also plausible that Ki67 and the lipid-containing components may function redundantly, at least
264 partially, thereby explaining several interesting observations. First, Ki67 is not an essential protein
265 but is a cell proliferation marker, with Ki67 knockout cells still proliferating under cultured
266 conditions [22]. Second, to date, Ki67 homologs have only been detected in vertebrates [40]. Proteins
267 homeologous to Ki67 have not been identified or characterized in any other non-vertebrate
268 eukaryotes. Our results indicate that nuclear lipids exert a novel role in isolating or individualizing
269 condensed sister chromatid pairs during mitosis of cultured mammalian cells. It would be
270 interesting to investigate further if nuclear lipids in non-vertebrate organisms also exhibit similar
271 functions.

272 Our results are consistent with previous reports [37, 38] showing that PS is mainly present in
273 epichromatin or on the outer surface of condensed chromosomes during mitosis (**Figure 4**). Using
274 biotin-DHPE, we show that nuclear lipids or lipid-containing components accumulate around the
275 periphery of entire chromosomes during mitosis (**Figure 4**). Mammalian nuclei contain a variety
276 of lipids, including PS, phosphatidylinositol, cholesterol, free fatty acids, diacylglycerol, and
277 sphingolipids [41]. Further investigations are needed to reveal if all these lipids or specific types of
278 lipids are enriched around the periphery of condensed chromosomes.

279 Lastly, our findings herein may provide a new perspective on mitosis in general. The NE,
280 which comprises two lipid bilayers, is a highly regulated membrane barrier that separates the
281 nucleus from the cytoplasm in eukaryotes. Depending on the organism and cell type, the NE
282 remains intact during closed mitosis or disassembles during open mitosis before chromosome

283 segregation. Closed mitosis occurs in many (but not all) fungi and is considered the most ancient
284 mechanism of eukaryotic cell division. In contrast, animals and plants undergo open mitosis, which
285 appears to have evolved independently several times [42]. A few fungi (e.g., the fission yeast
286 *Shizosaccharomyces japonicus* and the corn smut fungus *Ustilago maydis*) undergo semi-open
287 mitosis, in which the NE does not disassemble completely [43]. As yet, it is not fully understood why
288 open mitosis prevails in animals and plants, but not in fungi. The results from this study reveal that
289 Ki67 and nuclear lipids constitute a thin "chromosome envelope" around each sister chromatid
290 pair, with the transition from "nuclear envelope" to "chromosome envelope" enabling continued
291 isolation of genetic material from cytoplasmic material, thereby ensuring the individualization of
292 sister chromatid pairs, the formation of star-like microtubule arrays, and proper chromosome
293 segregation.
294

295 ## Methods

296 **Antibodies and reagents**

297 Rabbit polyclonal HSP90 was a kind gift from Dr. Chung Wang (Institute of Molecular Biology,
298 Academia Sinica). Commercially available antibodies and chemicals used in this report are as
299 follows: rat monoclonal Ki67 (SolA15, #14-569882, 1:2000 for immunoblotting, 1:500 for TT-
300 ExM, Invitrogen); mouse monoclonal phosphatidylserine (PS) (1H6, 05-719, 1:200 for TT-ExM,
301 Sigma-Aldrich); rabbit polyclonal α-Tubulin (ab18251, 1:500, Abcam); chicken polyclonal GFP
302 (ab13970, 1:1000 for TT-ExM, Abcam); mouse monoclonal GFP (JL-8, 632381, 1:2000 for
303 immunoblotting, Clontech); Alexa Fluor-488-, 555- and 647-conjugated secondary antibodies
304 (Invitrogen); Nocodazole (M1404, Sigma-Aldrich); DAPI (D1306,1:1000, Invitrogen); PicoGreen
305 (P11495, 1:1000, ThermoFisher). Reagents used for DHPE TT-ExM are as follows: N-(Biotinoyl)-

306 1,2-dihexadecanoyl-snglycero-3-phosphoethanolamine, triethylammonium salt (Biotin-DHPE)
307 (60022, 0.1mg/ml, Biotium); VECTASTAIN ABC-HRP Kit, peroxidase (standard), (PK-4000, Vector
308 Laboratory); Alexa fluor-555-conjugated tyramide (B40955, 1:100, Invitrogen); Amplification diluent
309 (FP1050, PerkinElmer); 6-((acryloyl)amino)hexanoic acid (Acryloyl-X, SE, A-20770,
310 ThermoFisher); Sodium acrylate (408220, Sigma-Aldrich); Acrylamide (A9099, Sigma-Aldrich);
311 N, N'-methylenebisacrylamide, (1551624, ThermoFisher); Ammonium persulfate, (APS, A9164,
312 Sigma-Aldrich); N,N,N,,N,-Tetramethylethylenediamine (TEMED, T7024, Sigma-Aldrich); 4-
313 Hydroxy-TEMPO (176141, Sigma-Aldrich); Sodium chloride (3624-69, J.T.Baker); Trypsin-
314 EDTA solution, 0.05% (25300-054, Gibco).
315
316 **Plasmid construction**
317 To generate the Ki67-miR knockdown constructs, an artificial miRNA was designed using
318 BLOCK-iT™ RNAi Designer (https://rnaidesigner.thermofisher.com/rnaiexpress/). According to
319 the ranking score, the top miRNA (nucleotide residues 3296-3319,
320 AAGAGCTTGCCTGATACAGAA) was chosen and cloned into pcDNA6.2-GW/EmGFP vector.
321 A control vector (pcDNA6.2–GW/EmGFP-miR, Invitrogen) expressing a scrambled miRNA [44]
322 predicted to not target any gene in mammalian genomes was used as the negative control in our
323 knockdown experiments.
324
325 **COS-7 culture and nocodazole treatment**
326 The monkey COS-7 fibroblast-like cell line (ATCC, CRL-1651) was maintained in DMEM
327 supplemented with 10% FBS, 1% penicillin/streptomycin and 2 mM glutamine. For mitotic cell cycle
328 analysis, cells were treated with 50 nM nocodazole for 6 h to synchronize the cell cycle in

329 prometaphase. Media were then washed out and the cells were allowed to recover for 15, 30, or 60
330 min to re-enter the mitotic cycle. Mitotic stages were identified based on chromosome patterning.
331
332 **Transfection and immunoblotting of COS-7 cells**
333 COS-7 cells were transfected with the indicated plasmids using PolyJet (SL100688, SignaGen
334 Laboratories) according to the manufacturer's instructions. For Ki67 knockdown analysis, the
335 transfection period was extended to 2 days to enhance knockdown efficiency. For immunoblotting
336 analysis, cells were washed with PBS twice and lysed directly with SDS sample buffer. Total cell
337 lysates were separated by means of SDS-PAGE and analyzed by immunoblotting.
338
339 **Immunofluorescence analysis**
340 Regular immunostaining was performed as described previously [44]. Briefly, cells were washed
341 with phosphate-buffered saline (PBS) and fixed with 4% paraformaldehyde (PFA) and 4% sucrose
342 in PBS for 10 min, followed by permeabilization with 0.2% Triton X-100 in PBS for 15 min at
343 room temperature. After blocking with 10% bovine serum albumin (BSA), the cells were incubated
344 with primary antibodies diluted in PBS containing 3% BSA and 0.1% horse serum at 4 °C
345 overnight. After washing with PBS several times, the cells were incubated with secondary
346 antibodies conjugated with Alexa Fluor-488, -555 or -647 (Invitrogen) and DNA dye for 2 h at
347 room temperature.
348
349 **Lipid staining**
350 Lipid labeling using biotin-DHPE [32] was performed before regular immunostaining. The cells were
351 washed with PBS and then treated with 0.1 mg/ml biotin-DHPE in 50% ethanol overnight at room

352 temperature. To detect biotin-DHPE, an equal amount of reagents A and B in the Vectastin ABC-
353 HRP kit (Vector Laboratory) was mixed in TBS (1:50 dilution) for at least 30 min. After washing
354 with PBS several times, the biotin-DHPE-labeled cells were incubated with premixed ABC
355 solution for 1 h. After washing with PBS, Alexa fluor-555-conjugated tyramide was diluted (1:50)
356 in amplification diluent and applied to the cells for 15 min. Following extensive washing, the
357 biotin-DHPE-stained cells were then deemed ready for regular immunostaining.
358
359 **TT-ExM**
360 Immunostained COS-7 cells, prepared as described above, were subjected to TT-ExM [32, 33]. After
361 staining, the cells were washed with PBS three times and then incubated with 0.1 mg/ml Acryloyl-
362 X, SE in PBS overnight at 4 °C. After washing three times with PBS, the coverslip with stained
363 cells was placed on acrylamide solution (with the cell-attached side facing down) at 37 °C for 2 h
364 for gelation. After gelation was completed, the hydrogel was immersed in trypsin digestion
365 solution (0.05 % volume dilution: 2 μl trypsin-EDTA solution in 4 ml low salt digestion buffer),
366 and then incubated at room temperature for at least 20 h with gently shaking. The digested hydrogel
367 was transferred to a 10-cm dish filled with excess Milli-Q water for free expansion for 2 h. The
368 expanded samples were then imaged at room temperature using an LSM980 laser scanning
369 confocal microscope equipped with Airyscan 2 multiplex mode SR-4Y. An LD LCI Plan-
370 Apochromate 40X/1.2 Imm Corr DIC M27 objective was used for Z-series image acquisition.
371
372 **Analyses of DHPE invasion, chromosomal layer patterning and chromosome area**
373 To quantify the immunoreactivities of DHPE signals in the intrachromosomal area, line scanning
374 was performed using the ImageJ/Fiji software. A 3 μm-wide line across the chromosome or

375 perichromosomal layer was drawn to quantify DHPE signals. The intersection of biotin-DHPE
376 signal and the chromosome boundary was set as a ratio of 1. The lowest ratio of biotin-DHPE was
377 identified as the lipid level in the intrachromosomal area. Ten individual chromosomes per cell
378 were quantified and averaged. For chromosomal layer analysis, post-expanded and LSM980-
379 acquired images were subjected to line scanning analysis across the perichromosomal layer. Line
380 histograms were used to exhibit the distribution pattern of pericromosomal components. Five
381 individual chromosomes per cell were quantified and averaged. For chromosome area analysis,
382 the area occupied by chromosomes was quantified based on DAPI signals using ImageJ/Fiji.
383

384 **Analysis of microtubule organization**

385 To analyze microtubule organization, cells were stained with α-tubulin to identify microtubule
386 filaments and then assessed by means of Sholl analysis (ImageJ/Fiji) [44, 45] to examine the extension
387 pattern of tubule filaments and to count the numbers of intersections. Total numbers of
388 intersections and microtubule filament tips were counted to represent microtubule organization.
389

390 **Quantification and statistical analysis**

391 To avoid potential personal bias, all data were collected and analyzed blindly by having other lab
392 members relabel the samples. For each experiment, 10 cells were randomly collected from at least
393 two independent experiments for quantification. To analyze DHPE invasion into the chromosomal
394 area, line scanning analysis was performed at each mitotic stage using the ImageJ/FIJI software.
395 To analyze microtubule organization, Sholl analysis was performed in the ImageJ/FIJI software to
396 calculate numbers of microtubule filaments and their distribution patterns. Two-group
397 comparisons were analyzed with two-tailed unpaired Student's *t*-test. For more than two group

comparisons, a one-way analysis of variance (ANOVA) with Bonferroni's multiple comparison post-hoc test was performed.

Declarations

Ethics approval and consent to participate

Not applicable.

Consent for publication

All authors have read and approved of its submission to this journal.

Availability of data and materials

All relevant data are within the paper and its Supporting information files. The file of Supplemental Table S1 contains the numerical data for all figures. Supplemental Table S2 contains all statistical results. Supplemental Figure S1 contains uncropped blots of **Figure 5B**.

Competing interests

The authors declare no conflicts of interest.

Funding

Institute of Molecular Biology, Academia Sinica, Taiwan, Republic of China; and Academia Sinica, Taiwan, Republic of China [ASIA-111-L01 and AS-TP-110-L10 to Y.-P.H. and B.-C.C.]; National Science and Technology Council, Taiwan, Republic of China [NSTC 110-2811-B-001-542 to TFW; NSTC 108-2311-B-001-008-MY3 and 112-2326-B-001-008 to Y.-P.H.].

421

422 **Authors' contributions**

423 Conceptualization: YPH, TFW; Funding acquisition: YPH, TFW; Investigation: HTH, UTTW,
424 BCC, YPH; Methodology: HTH, UTTW, BCC, YPH, TFW; Project administration: YPH, TFW;
425 Supervision: YPH, TFW; Visualization: HTH, YPH; Writing – original draft: HTH, YPH, TFW;
426 Writing – review and editing: HTH, UTTW, BCC, YPH, TFW. All of the authors read and approved
427 the manuscript.

428

429 **Acknowledgements**

430 We thank the Imaging Core Facility of the Institute of Molecular Biology, Academia Sinica, for
431 technical support and John O'Brien for English editing.

432

433 **Authors' information**

434 Hisao-Tang Hu: annebest999@gmail.com

435 Ueh-Ting Tim Wang: 010118@gs.hs.ntnu.edu.tw

436 Bi-Chang Chen: chenb10@gate.sinica.edu.tw

437 Yi-Ping Hsueh: yph@gate.sinica.edu.tw

438 Ting-Fang Wang: tfwang@gate.sinica.edu.tw

439

440

441 ## References

442 1. Ledeen, R.W. & Wu, G. Nuclear sphingolipids: metabolism and signaling. *J Lipid Res* **49**,
443 1176-1186 (2008).
444 2. Garcia-Gil, M. & Albi, E. Nuclear Lipids in the Nervous System: What they do in Health
445 and Disease. *Neurochem Res* **42**, 321-336 (2017).
446 3. Moriel-Carretero, M. The Many Faces of Lipids in Genome Stability (and How to Unmask
447 Them). *Int J Mol Sci* **22** (2021).
448 4. Payrastre, B. *et al.* A differential location of phosphoinositide kinases, diacylglycerol
449 kinase, and phospholipase C in the nuclear matrix. *J Biol Chem* **267**, 5078-5084 (1992).
450 5. Vann, L.R., Wooding, F.B., Irvine, R.F. & Divecha, N. Metabolism and possible
451 compartmentalization of inositol lipids in isolated rat-liver nuclei. *Biochem J* **327 (Pt 2)**,
452 569-576 (1997).
453 6. Romanauska, A. & Köhler, A. The Inner Nuclear Membrane Is a Metabolically Active
454 Territory that Generates Nuclear Lipid Droplets. *Cell* **174**, 700-715.e718 (2018).
455 7. Fujimoto, T. Nuclear lipid droplets - how are they different from their cytoplasmic siblings?
456 *J Cell Sci* **135** (2022).
457 8. Osborne, S.L., Thomas, C.L., Gschmeissner, S. & Schiavo, G. Nuclear PtdIns(4,5)P2
458 assembles in a mitotically regulated particle involved in pre-mRNA splicing. *J Cell Sci* **114**,
459 2501-2511 (2001).
460 9. Mortier, E. *et al.* Nuclear speckles and nucleoli targeting by PIP2-PDZ domain interactions.
461 *Embo j* **24**, 2556-2565 (2005).
462 10. Wang, Y.-H. *et al.* DNA damage causes rapid accumulation of phosphoinositides for
463 ATR signaling. *Nature Communications* **8**, 2118 (2017).

464 11. Zou, C. *et al.* Acyl-CoA:lysophosphatidylcholine acyltransferase I (Lpcat1) catalyzes
465 histone protein O-palmitoylation to regulate mRNA synthesis. *J Biol Chem* **286**, 28019-
466 28025 (2011).
467 12. Yildirim, S. *et al.* Involvement of phosphatidylinositol 4,5-bisphosphate in RNA
468 polymerase I transcription. *J Cell Sci* **126**, 2730-2739 (2013).
469 13. McDonnell, E. *et al.* Lipids Reprogram Metabolism to Become a Major Carbon Source for
470 Histone Acetylation. *Cell Rep* **17**, 1463-1472 (2016).
471 14. Zhang, X.H., Zhao, C. & Ma, Z.A. The increase of cell-membranous phosphatidylcholines
472 containing polyunsaturated fatty acid residues induces phosphorylation of p53 through
473 activation of ATR. *J Cell Sci* **120**, 4134-4143 (2007).
474 15. Cermelli, S., Guo, Y., Gross, S.P. & Welte, M.A. The lipid-droplet proteome reveals that
475 droplets are a protein-storage depot. *Curr Biol* **16**, 1783-1795 (2006).
476 16. Kumanski, S., Viart, B.T., Kossida, S. & Moriel-Carretero, M. Lipid Droplets Are a
477 Physiological Nucleoporin Reservoir. *Cells* **10** (2021).
478 17. Andrés-Sánchez, N., Fisher, D. & Krasinska, L. Physiological functions and roles in cancer
479 of the proliferation marker Ki-67. *J Cell Sci* **135** (2022).
480 18. Sun, X. & Kaufman, P.D. Ki-67: more than a proliferation marker. *Chromosoma* **127**, 175-
481 186 (2018).
482 19. Kill, I.R. Localisation of the Ki-67 antigen within the nucleolus. Evidence for a fibrillarin-
483 deficient region of the dense fibrillar component. *J Cell Sci* **109 (Pt 6)**, 1253-1263 (1996).
484 20. Booth, D.G. & Earnshaw, W.C. Ki-67 and the Chromosome Periphery Compartment in
485 Mitosis. *Trends Cell Biol* **27**, 906-916 (2017).

486 21. Gautier, T., Masson, C., Quintana, C., Arnoult, J. & Hernandez-Verdun, D. The
487 ultrastructure of the chromosome periphery in human cell lines. An in situ study using
488 cryomethods in electron microscopy. *Chromosoma* **101**, 502-510 (1992).
489 22. Cuylen, S. *et al.* Ki-67 acts as a biological surfactant to disperse mitotic chromosomes.
490 *Nature* **535**, 308-312 (2016).
491 23. Cuylen-Haering, S. *et al.* Chromosome clustering by Ki-67 excludes cytoplasm during
492 nuclear assembly. *Nature* **587**, 285-290 (2020).
493 24. Ma, N. *et al.* Nucleolin functions in nucleolus formation and chromosome congression. *J*
494 *Cell Sci* **120**, 2091-2105 (2007).
495 25. Hsu, T.C., Arrighi, F.E., Klevecz, R.R. & Brinkley, B.R. The nucleoli in mitotic divisions
496 of mammalian cells in vitro. *J Cell Biol* **26**, 539-553 (1965).
497 26. Moyne, G. & Garrido, J. Ultrastructural evidence of mitotic perichromosomal
498 ribonucleoproteins in hamster cells. *Exp Cell Res* **98**, 237-247 (1976).
499 27. Ma, K. *et al.* Ribosomal RNA regulates chromosome clustering during mitosis. *Cell*
500 *Discovery* **8**, 51 (2022).
501 28. Guillen-Chable, F., Bayona, A., Rodríguez-Zapata, L.C. & Castano, E. Phase Separation
502 of Intrinsically Disordered Nucleolar Proteins Relate to Localization and Function. *Int J*
503 *Mol Sci* **22** (2021).
504 29. Morovicz, A.P. *et al.* Phosphoinositide 3-kinase signalling in the nucleolus. *Adv Biol Regul*
505 **83**, 100843 (2022).
506 30. Chen, F., Tillberg, P.W. & Boyden, E.S. Optical imaging. Expansion microscopy. *Science*
507 **347**, 543-548 (2015).

508 31. Wassie, A.T., Zhao, Y. & Boyden, E.S. Expansion microscopy: principles and uses in
509 biological research. *Nat Methods* **16**, 33-41 (2019).
510 32. Wang, U.-T.T. *et al.* Protein and lipid expansion microscopy with trypsin and tyramide
511 signal amplification for 3D imaging. *Scientific Reports* **13**, 21922 (2023).
512 33. Hu, H.T. *et al.* Autism-related KLHL17 and SYNPO act in concert to control activity-
513 dependent dendritic spine enlargement and the spine apparatus. *PLoS Biol* **21**, e3002274
514 (2023).
515 34. Chang, J.B. *et al.* Iterative expansion microscopy. *Nat Methods* **14**, 593-599 (2017).
516 35. M'Saad, O. & Bewersdorf, J. Light microscopy of proteins in their ultrastructural context.
517 *Nat Commun* **11**, 3850 (2020).
518 36. Louvel, V. *et al.* iU-ExM: nanoscopy of organelles and tissues with iterative ultrastructure
519 expansion microscopy. *Nat Commun* **14**, 7893 (2023).
520 37. Prudovsky, I., Vary, C.P., Markaki, Y., Olins, A.L. & Olins, D.E. Phosphatidylserine
521 colocalizes with epichromatin in interphase nuclei and mitotic chromosomes. *Nucleus* **3**,
522 200-210 (2012).
523 38. Gould, T.J. *et al.* Defining the epichromatin epitope. *Nucleus* **8**, 625-640 (2017).
524 39. Sholl, D.A. Dendritic organization in the neurons of the visual and motor cortices of the
525 cat. *J Anat* **87**, 387-406 (1953).
526 40. Remnant, L., Kochanova, N.Y., Reid, C., Cisneros-Soberanis, F. & Earnshaw, W.C. The
527 intrinsically disorderly story of Ki-67. *Open Biol* **11**, 210120 (2021).
528 41. Ledeen, R.W. & Wu, G. Nuclear lipids: key signaling effectors in the nervous system and
529 other tissues1. *Journal of Lipid Research* **45**, 1-8 (2004).

530 42. Cavalier-Smith, T. Origin of the cell nucleus, mitosis and sex: roles of intracellular
531 coevolution. *Biol Direct* **5**, 7 (2010).
532 43. Boettcher, B. & Barral, Y. The cell biology of open and closed mitosis. *Nucleus* **4**, 160-165
533 (2013).
534 44. Hu, H.T., Huang, T.N. & Hsueh, Y.P. KLHL17/Actinfilin, a brain-specific gene associated
535 with infantile spasms and autism, regulates dendritic spine enlargement. *J Biomed Sci* **27**,
536 103 (2020).
537 45. Chen, C.Y., Lin, C.W., Chang, C.Y., Jiang, S.T. & Hsueh, Y.P. Sarm1, a negative regulator
538 of innate immunity, interacts with syndecan-2 and regulates neuronal morphology. *J Cell*
539 *Biol* **193**, 769-784 (2011).
540

541 **Figures and Figure Legends**

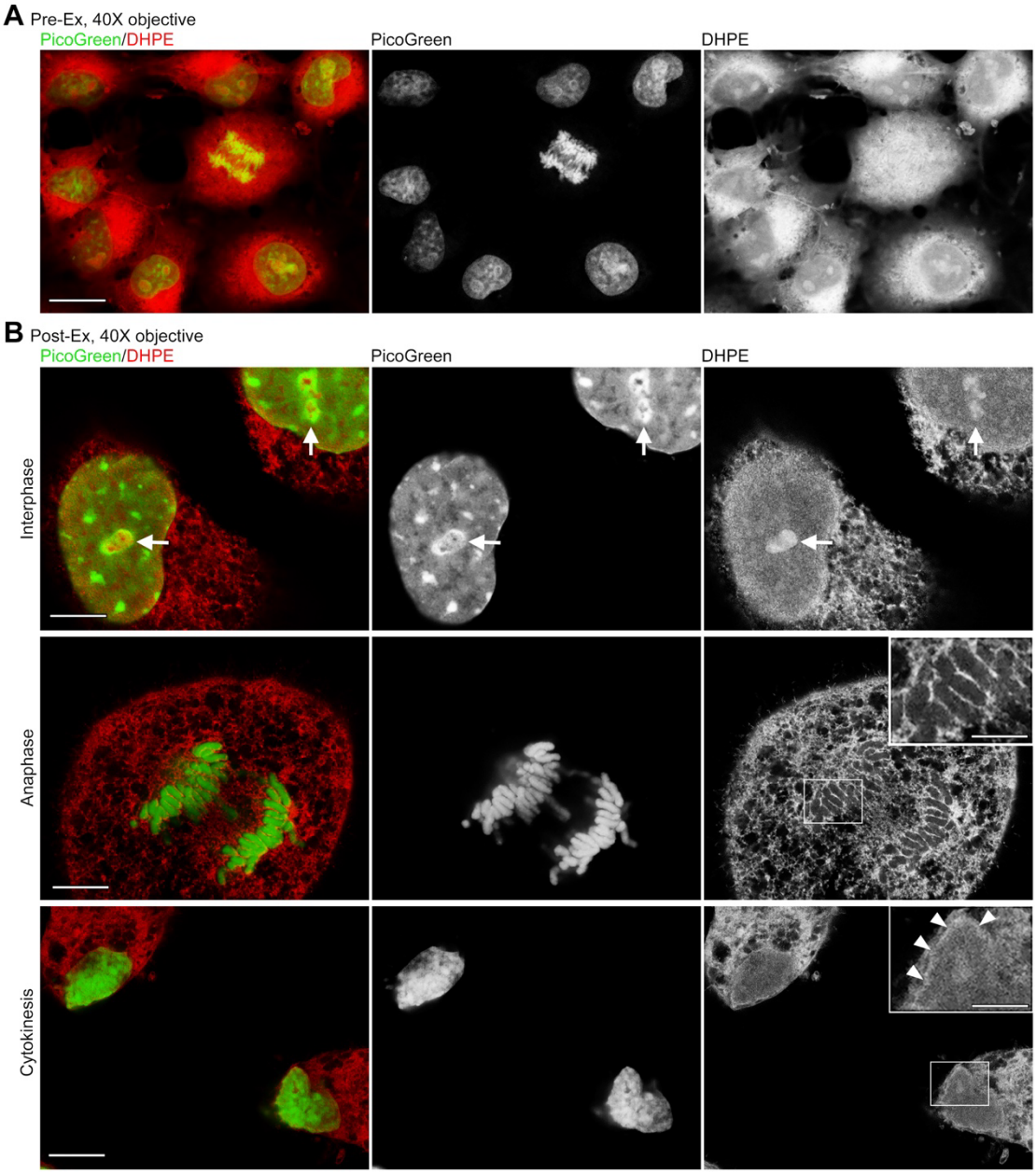

542

543 **Figure 1.** TT-ExM reveals the distribution of lipids and DNA throughout the cell cycle.
544 COS-7 cells were subjected to TT-ExM with staining using biotin-DHPE and PicoGreen. Images
545 were acquired using an LSM700 confocal microscope. (**A**) Confocal images of cells before
546 expansion (Pre-Ex). (**B**) Confocal images of cells after expansion (Post-Ex). Different stages of
547 the cell cycle are shown. Arrows indicate the biotin-DHPE signals located in the nucleolus during
548 interphase. The enlarged chromosome segment shows the enriched biotin-DHPE signals at the

549 perichromosomal layers during anaphase. Arrowheads indicate the reforming nuclear envelope
550 after telophase. Scale bars: (**A**) 20 μm; (**B**) whole cells: 20 μm; enlarged segment: 8 μm.

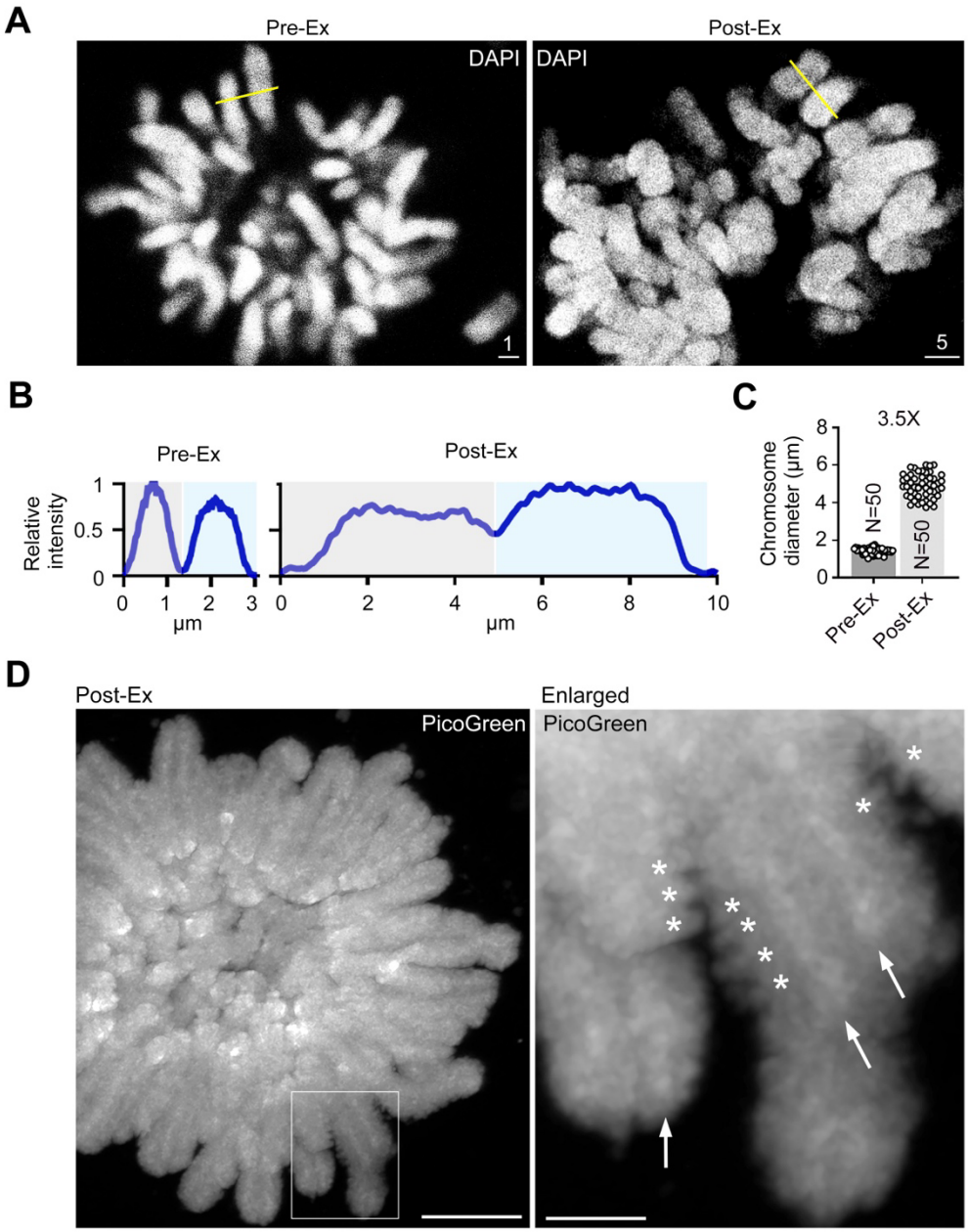

Figure 2. Chromosomal DNA expands isotropically in prometaphase.

COS-7 cells were subjected to TT-ExM using PicoGreen or DAPI for DNA staining. Images were acquired using an LSM980 confocal microscope with an Airyscan2 detector. (**A**) Representative images of mitotic chromosomes in prometaphase before and after expansion. Yellow lines are examples of the perpendicular line drawn for line scanning analysis. (**B**)-(**C**) Quantification of chromosome diameters in Pre-Ex and Post-Ex cells. Light grey and blue blocks indicate the regions of two adjacent chromosomes for measurement. Expansion was determined to be 3.5-fold. (**D**) Confocal images of PicoGreen signals in entire Post-Ex cells and enlarged chromosome segments.

560 PicoGreen signal revealed likely chromosome axes displaying a denser DNA signal (arrows), as
561 well as chromosomal loops (asterisks). Scale bars: (**A**) pre-Ex: 1 µm; post-Ex: 5 µm; (**B**) whole
562 cells: 10 µm; enlarged segment: 2.5 µm.
563

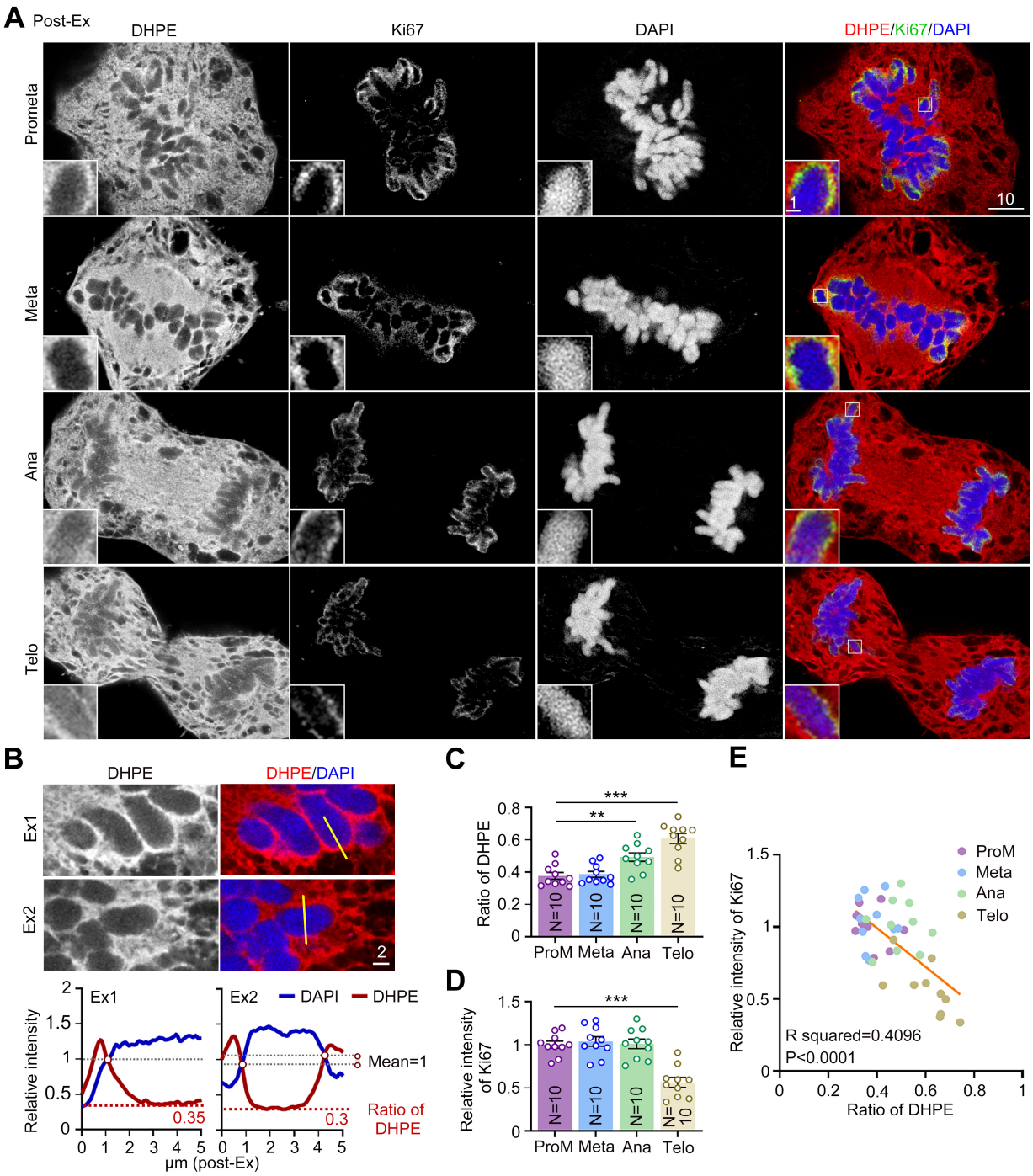

Figure 3. Distribution patterns of Ki67 and biotin-DHPE signals during mitosis. COS-7 cells were subjected to TT-ExM and stained using biotin-DHPE, Ki67 antibody and DAPI. Images at different mitotic stages were acquired using an LSM980 confocal microscope with Airyscan2. (**A**) Confocal images of entire cells and enlarged chromosome segments at different stages of mitosis: Prometa (prometaphase); Meta (metaphase); Ana (anaphase); Telo (telophase). The original regions of the enlarged images are indicated only in the rightmost panels. (**B**) Line

571 scanning analysis of biotin-DHPE distribution across the perichromosomal layer and chromosome.
572 Yellow lines indicate the regions analyzed in the two examples, Ex1 and Ex2. Lower panel: The
573 results of line scanning analysis on Ex1 and Ex2. The red open circles indicate the intersection of
574 biotin-DHPE signal and the chromosome boundary, which was set as a ratio of 1. The lowest ratio
575 of biotin-DHPE was identified as the relative lipid level in the chromosome interior. (**C**) Ratio of
576 the biotin-DHPE signal in the intrachromosomal area to that at the periphery. The ratio was lower
577 in prometaphase and metaphase, but increased in anaphase and telophase. (**D**) Relative levels of
578 total Ki67 immunoreactivity, which clearly declined during telophase. (**E**) Negative correlation of
579 the biotin-DHPE ratio and Ki67 signal intensity. The sample size "N" indicates the number of
580 examined cells. The data represent mean ± SEM and individual data points are also shown. All
581 data were collected from at least two independent experiments. ** $P < 0.01$; *** $P < 0.001$; one-
582 way ANOVA. Scale bars: (**A**) whole cells: 10 μm; enlarged segment: 1 μm; (**B**) 2 μm.
583

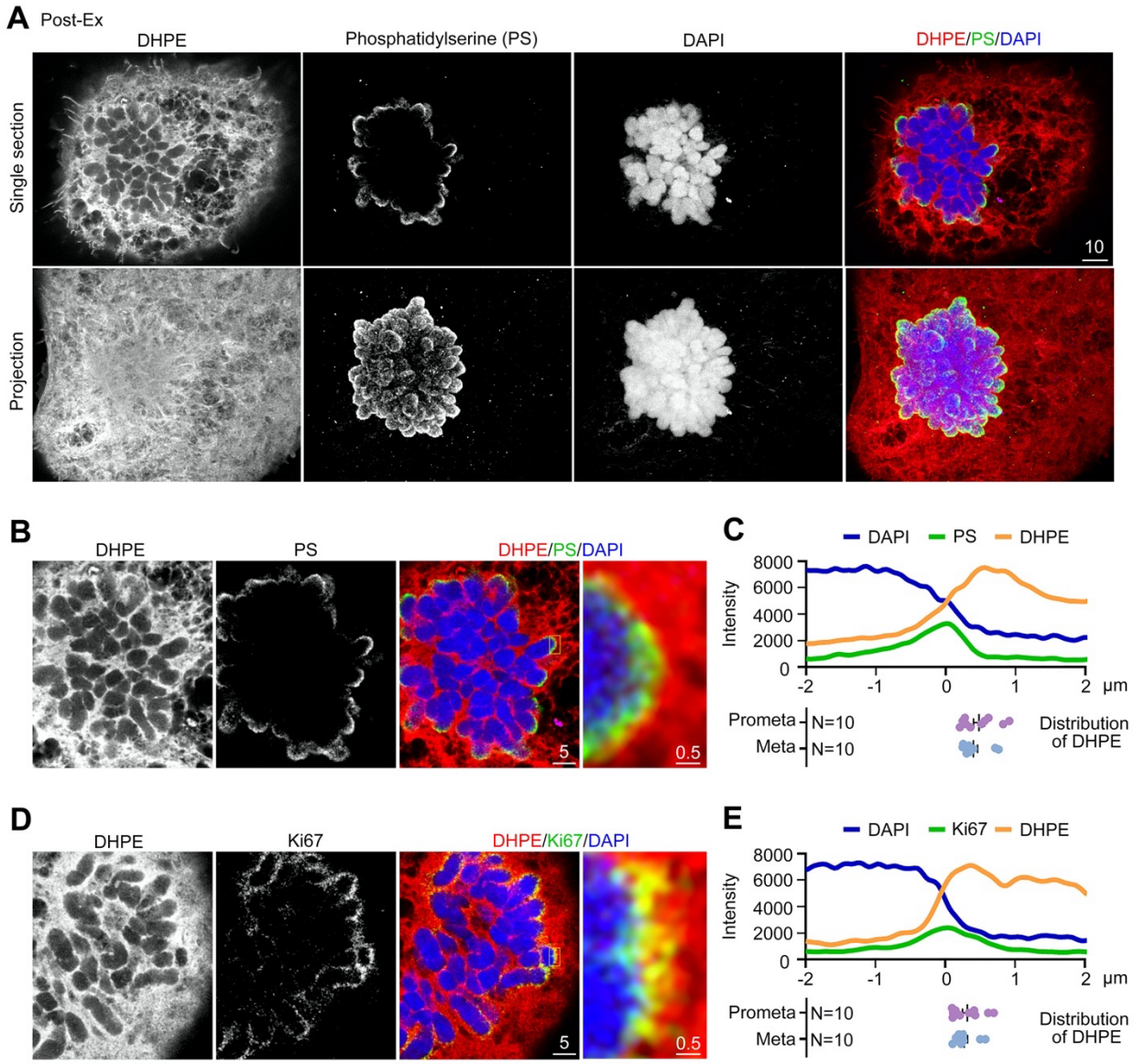

Figure 4. Relative distribution patterns of Ki67, biotin-DHPE and PS.

COS-7 cells were subjected to TT-ExM and stained using antibodies recognizing Ki67 and phosphatidylserine (PS), as well as for biotin-DHPE and DAPI. Images of cells in prometaphase and metaphase were acquired using an LSM980 microscope with an AiryScan2 detector. (**A**) Confocal images of lipid components (biotin-DHPE and PS) during prometaphase. Upper: Single section. Lower: Z-projection. Biotin-DHPE was distributed throughout cells and covered the entire chromosomes. PS was only located in regions of epichromatin. (**B**)-(**C**) Distribution of biotin-DHPE and PS. (**D**)-(**E**) Distribution of biotin-DHPE and Ki67. **(B), (D)** Representative confocal images. The 10X enlarged images of the insets at regions of epichromatin in the whole-cell images are shown in the rightmost panels. **(C), (E)** The results of line scanning. Upper: an example of the

595 line scanning result. Lower: the relative positions of the peaks of biotin-DHPE signals. The peaks
596 of PS and Ki67 signals at the chromosome edge are set as 0. Biotin-DHPE signals are always
597 present at the outer part of perichromosomal layer relative to the PS and Ki67 signals. The sample
598 size "N" indicates the number of examined cells in prometaphase and metaphase. Scale bars: (**A**)
599 10 μm; (**B**), (**D**) whole cells: 5 μm; enlarged segment: 0.5 μm.
600

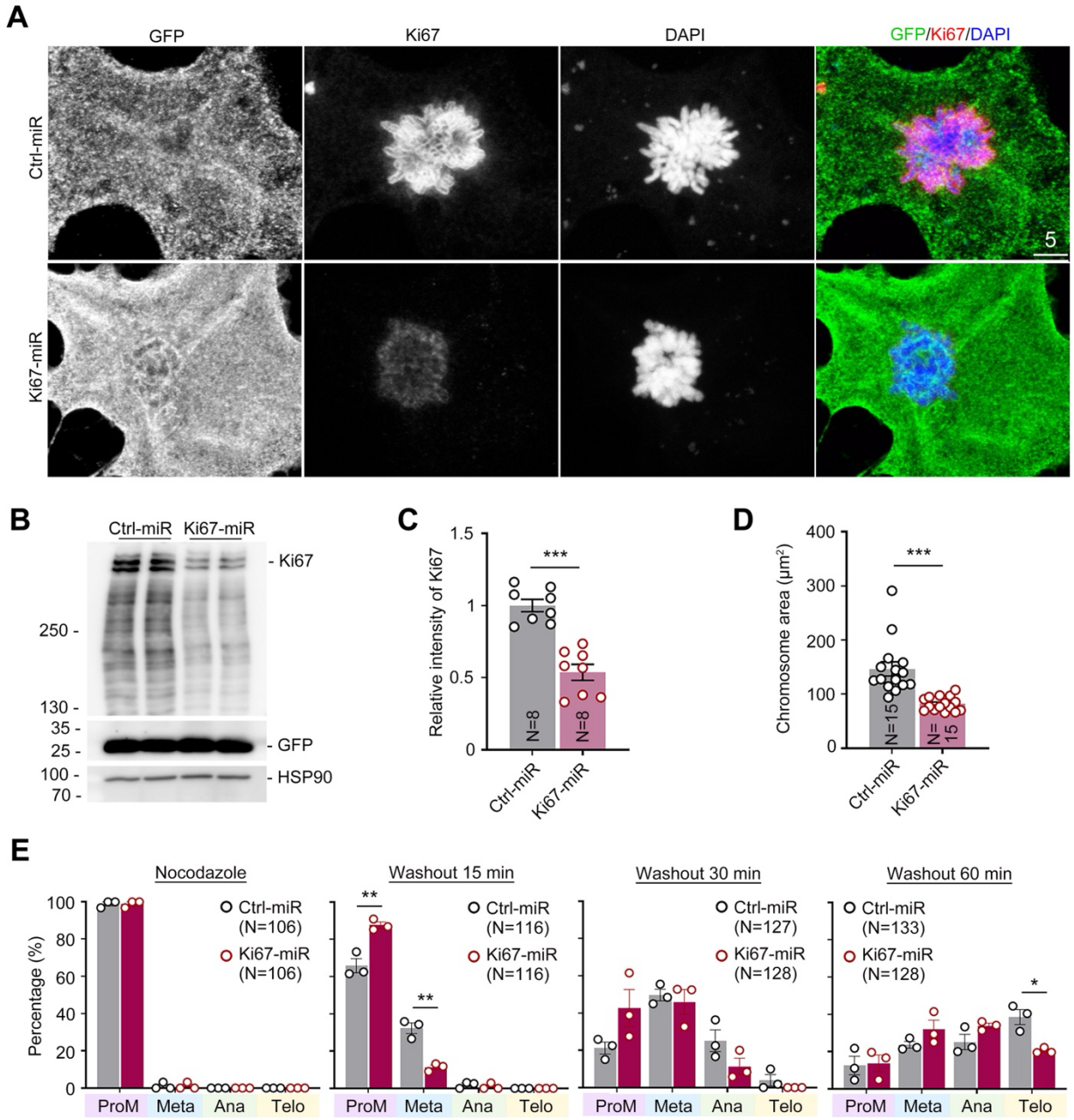

Figure 5. Ki67 knockdown alters chromosome structure and delays mitotic progress. COS-7 cells were transfected with Ki67-miR or Ctrl-miR and then stained with Ki67 antibody and DAPI. Since miR constructs coexpress GFP, GFP signals were used to label transfected cells. Images were acquired using an LSM700 confocal microscope. (**A**) Representative confocal images in prometaphase. Ki67 signal intensity (**C**) and chromosome areas (**D**) were analyzed for transfected cells. (**B**) The knockdown effect of Ki67-miR. Whole-cell extracts were collected and immunoblotted with Ki67 antibody to detect endogenous Ki67 protein levels. GFP and HSP90 are

609 loading controls. (**C**) The relative Ki67 signals in Ki67-miR- and Ctrl-miR-expressing cells. (**D**)
610 Loss of Ki67 reduces chromosome area. (**E**) Ki67 knockdown delays progress of mitosis. Cells
611 were treated with 50 nM nocodazole for 6 h to synchronize the cell cycle at prometaphase. After
612 removing nocodazole, the cells were allowed to recover for 15, 30 or 60 mins before being
613 harvested for immunostaining. Mitotic stages were determined according to chromosome
614 patterning. The sample sizes (N) of independent preparations (**C**) or examined cells (**D**, **E**) are
615 indicated in the panels. In (**E**), total cell numbers were collected from three independent
616 experiments. The data represent mean ± SEM and individual data points are also shown. All data
617 were collected from at least two independent experiments. * $P < 0.05$; ** $P < 0.01$; *** $P < 0.001$;
618 two-tailed unpaired Student's *t*-test. Scale bars: (**A**) 5 μm.
619

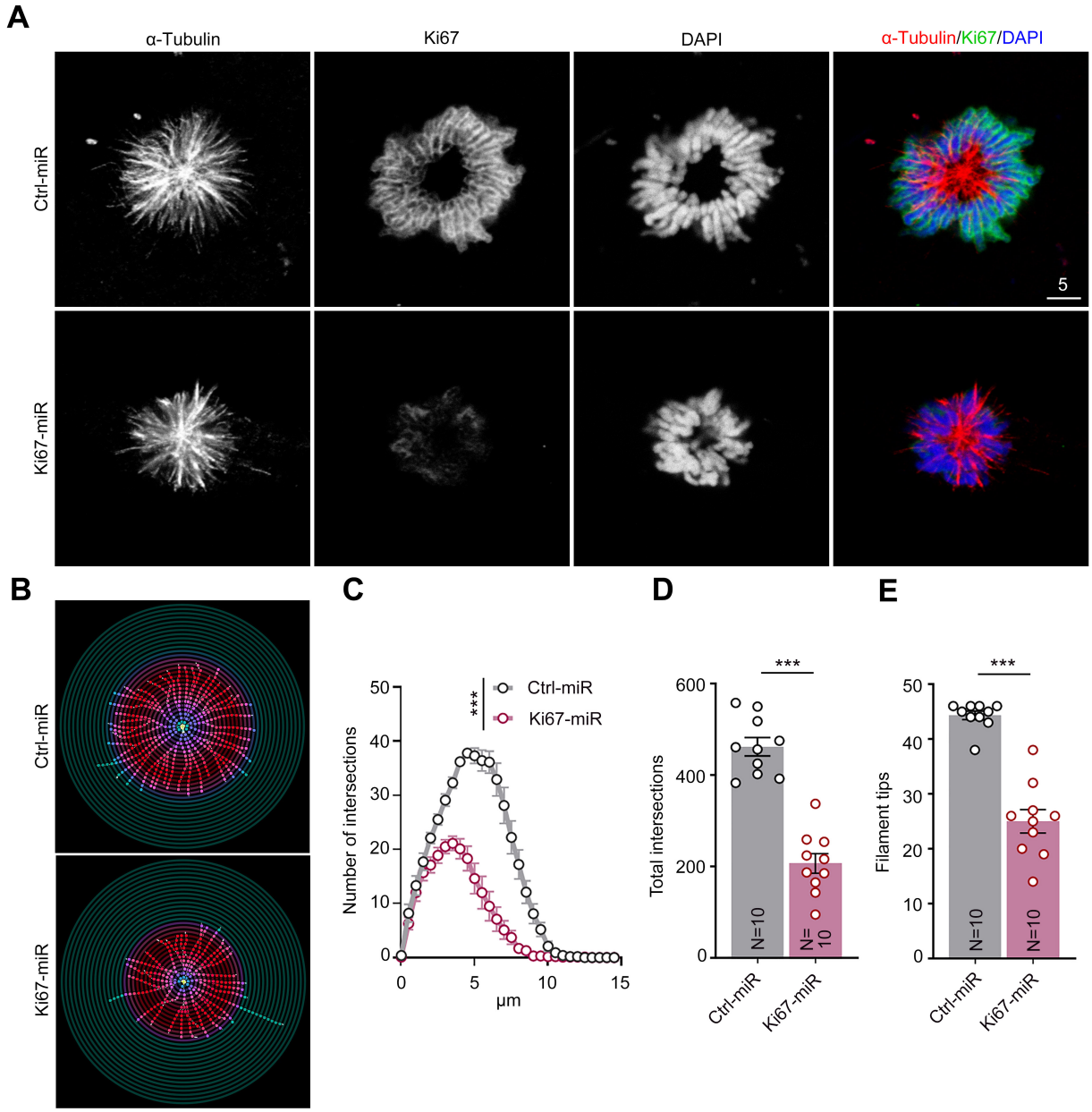

Figure 6. Loss of Ki67 disturbs microtubule organization.

COS-7 cells were transfected with Ki67-miR or Ctrl-miR plasmids and stained with Ki67 and α-tubulin (for microtubule) antibodies and DAPI. Images were acquired using an LSM700 confocal microscope. (**A**) Confocal images of microtubule filaments during prometaphase. Representative images of Crtl-miR- and Ki67-miR-expressing cells are shown. (**B**)-(**E**) Quantification of microtubule organization by Sholl analysis. (**B**) Representative images of Sholl analysis. (**C**) The distribution of numbers of intersections. (**D**) Total numbers of intersections. (**E**) Total numbers of microtubule filament tips. The sample size "N" indicates the number of examined cells. The data

represent mean ± SEM and individual data points are also shown. All data were collected from two independent experiments. *** $P < 0.001$; two-tailed unpaired Student's *t*-test. Scale bars: **(A)** 5 μm.

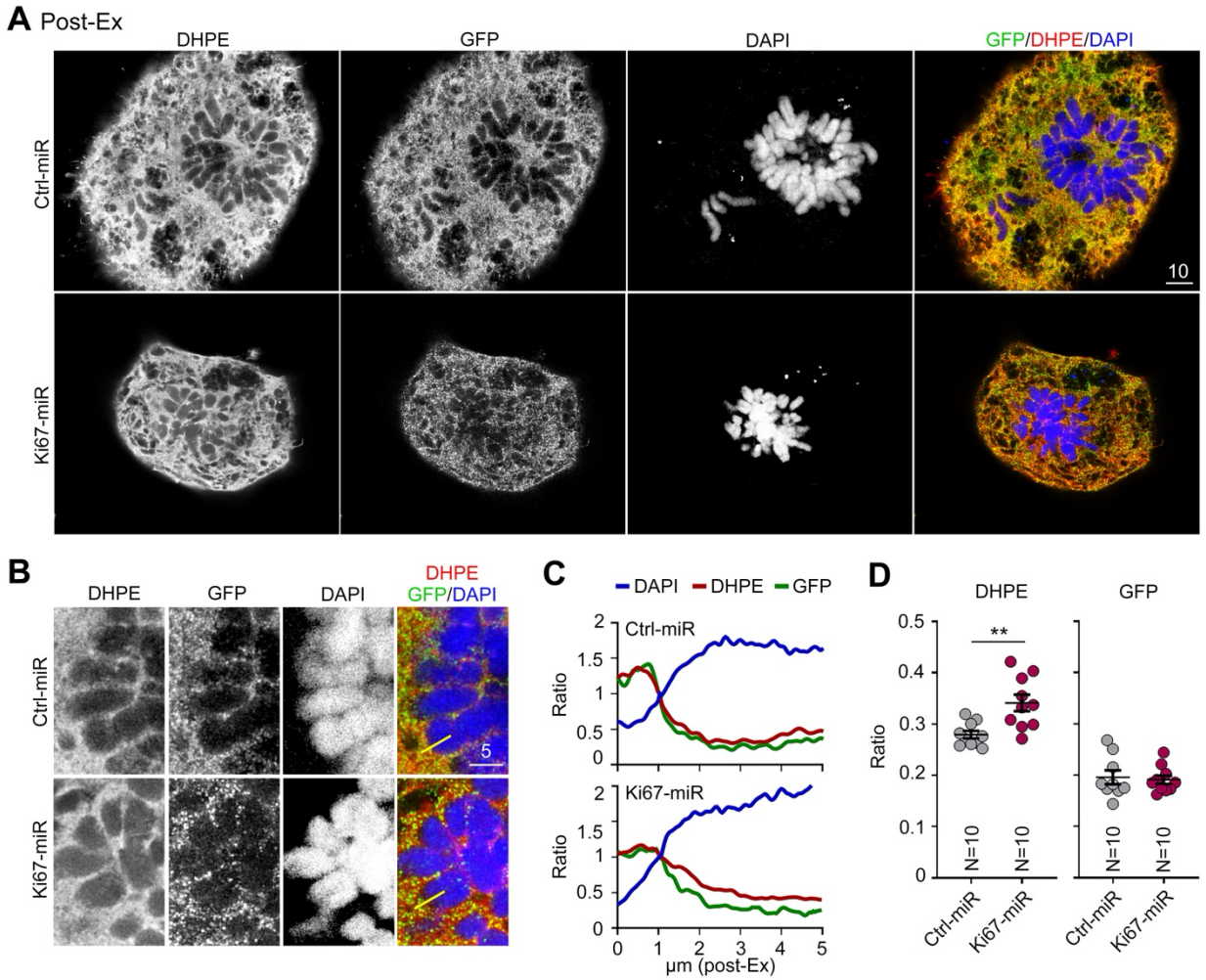

Figure 7. Lipid distribution is altered by Ki67 knockdown.

COS-7 cells were transfected with Ki67-miR or Ctrl-miR plasmids and then stained with biotin-DHPE, Ki67 antibody and DAPI for TT-ExM. An LSM980 microscope with an AiryScan2 detector was used to acquire images of the cells in prometaphase. (**A**) Representative confocal images. (**B**)-(**D**) Line scanning analysis reveals a change in biotin-DHPE distribution. The yellow lines indicate the regions subjected to line scanning. GFP serves as a control that is insensitive to Ki67 knockdown. The sample size "N" indicates the number of examined cells. The data represent mean ± SEM and individual data points are also shown. All data were collected from at least two dependent experiments. ** $P < 0.01$; two-tailed unpaired Student's *t*-test. Scale bars: (**A**) 10 μm; (**B**) 5 μm.